

Supplemental Material for “Magnetic Field Fingerprinting of Integrated Circuit Activity with a Quantum Diamond Microscope”

Matthew J. Turner,^{1,2} Nicholas Langellier,^{1,3} Rachel Bainbridge,⁴ Dan Walters,⁴
Srujan Meesala,^{1,*} Thomas M. Babinec,⁵ Pauli Kehayias,⁶ Amir Yacoby,^{1,5} Evelyn
Hu,⁵ Marko Lončar,⁵ Ronald L. Walsworth,^{1,2,3,7,8,9} and Edlyn V. Levine^{1,4,†}

¹*Department of Physics, Harvard University, Cambridge, MA 02138, USA*

²*Center for Brain Science, Harvard University, Cambridge, MA 02138, USA*

³*Harvard-Smithsonian Center for Astrophysics, Cambridge, MA 02138, USA*

⁴*The MITRE Corporation, Bedford, MA 01730, USA*

⁵*John A. Paulson School of Engineering and Applied Sciences,
Harvard University, Cambridge, Massachusetts 02138, United States*

⁶*Sandia National Laboratories, Albuquerque, NM 87123, USA*

⁷*Department of Physics, University of Maryland, College Park, MD 20742, USA*

⁸*Department of Electrical and Computer Engineering, University of Maryland, College Park, MD 20742, USA*

⁹*Quantum Technology Center, University of Maryland, College Park, MD 20742, USA*

(Dated: June 12, 2020)

CONTENTS

I. Supplemental Sections	1
A. Electric Field Terms	2
B. Simplification of Resonance Frequencies	2
C. Lorentzian Function	2
D. Multimodal Imaging: Magnetic Field, Contrast, Linewidth, and Temperature	3
E. Device Under Test Details	4
F. State Dependent Current Delivery to Development Board	4
G. Measured Noise Floor	5
H. Measurement Duration and Sensitivity	5
I. Magnetic Field Image Slices	7
J. Vector Magnetic Field Measurements of Additional Active Regions	7
K. Larger Measurement Stand-off Distance Using a 40 micron NV Layer	7
L. COMSOL Simulations	8
M. Data for Low Number Active RO States	9
N. Explained Variance of Principal Components	10
O. Relative Importance of Each Principal Component	11
P. Additional PC Score Plots	13
Q. Hyperparameter Cross Validation	13
R. Noise Propagation in PCA	15
References	16

I. SUPPLEMENTAL SECTIONS

This supplemental material provides additional information on the experimental procedures, data analysis, and interpretation of results presented in the main text. We include additional measurements and simulations taken to support our main conclusions.

* Current Affiliation: Thomas J. Watson, Sr. Laboratory of Applied Physics, California Institute of Technology, Pasadena, California 91125, USA

† Corresponding Author: edlynlevine@fas.harvard.edu

A. Electric Field Terms

Electric field terms are neglected in the NV Hamiltonian presented in the main text due to their minimal contribution to the present study. The interaction between an external electric field and the NV^- electronic spin state is described by the ground state Hamiltonian [S1]

$$H_{E-field} \approx d_{\parallel} E_z S_z + d_{\perp} E_x (S_y^2 - S_x^2) + d_{\perp} E_y (S_x S_y + S_y S_x) \quad (S1)$$

Electric fields couple weakly to the NV ground state Hamiltonian due to the relatively small dipole moments $d_{\parallel} \approx 3.5 \times 10^{-3}$ Hz/(V/m) and $d_{\perp} \approx 0.17$ Hz/(V/m) [S1, S2]. Similarly to the stress contribution to the Hamiltonian, the perpendicular components of the electric field are suppressed by the application of an on-axis bias magnetic field B_z [S2].

Consider an extreme situation where a changing chip function causes a change in potential of 1 V between traces separated by $10 \mu m$. The resulting electric field in the gap between the traces is of the order 10^5 V/m. For on-axis electric field components this would lead to shifts in the NV zero-field splitting of 350 Hz. In addition, using the known temperature dependence of the NV zero-field splitting, $\partial D/\partial T \approx -74$ kHz/C [S3], this electric field induced shift of 350 Hz appears equivalent to a temperature change of 5×10^{-4} °C. The electric field contribution is consequently insignificant, and is thus neglected from the analysis in the main text.

B. Simplification of Resonance Frequencies

Equations 4, 5, and 6 of the main text proceed from the analysis presented in [S4] with the following simplifying assumptions and simplifications. Treating the off-axis magnetic fields as perturbative, the difference between the active and idle state ODMR resonance frequencies is given by [S4]:

$$f_{\pm,i,Active} - f_{\pm,i,Idle} \approx \left(D + M_z + \frac{\partial D}{\partial T} \Delta T \right) + \frac{3\gamma^2 [(B_x + \Delta B_x)^2 + (B_y + \Delta B_y)^2]}{2(D + M_z + \frac{\partial D}{\partial T} \Delta T)} \pm \gamma(B_z + \Delta B_z) - (D + M_z) - \frac{3\gamma^2 (B_x^2 + B_y^2)}{2(D + M_z)} \mp \gamma B_z \quad (S2)$$

In the limit of $D \gg \frac{\partial D}{\partial T} \Delta T$, M_z the denominators in the off-axis magnetic field terms simplify to $2D$, giving

$$f_{\pm,i,Active} - f_{\pm,i,Idle} \approx \left(D + M_z + \frac{\partial D}{\partial T} \Delta T \right) + \frac{3\gamma^2 [(B_x + \Delta B_x)^2 + (B_y + \Delta B_y)^2]}{2D} \pm \gamma(B_z + \Delta B_z) - (D + M_z) - \frac{3\gamma^2 (B_x^2 + B_y^2)}{2D} \mp \gamma B_z = \frac{\partial D}{\partial T} \Delta T + \frac{3\gamma^2 [2B_x \Delta B_x + \Delta B_x^2 + 2B_y \Delta B_y + \Delta B_y^2]}{2D} \pm \gamma \Delta B_z \quad (S3)$$

Terms on the order ΔB_x^2 and ΔB_y^2 are negligible and can be ignored, as are terms dependent on off-axis magnetic fields given that $\frac{\gamma B_x}{D} < 10^{-2}$. These terms only impact the common mode splitting (i.e., temperature measurements) and do not couple into measurements of B_z to first order, allowing for a further simplification to

$$\Delta f_{\pm,i} = f_{\pm,i,Active} - f_{\pm,i,Idle} \approx \frac{\partial D}{\partial T} \Delta T \pm \gamma \Delta B_z \quad (S4)$$

which is the result presented in the main text.

C. Lorentzian Function

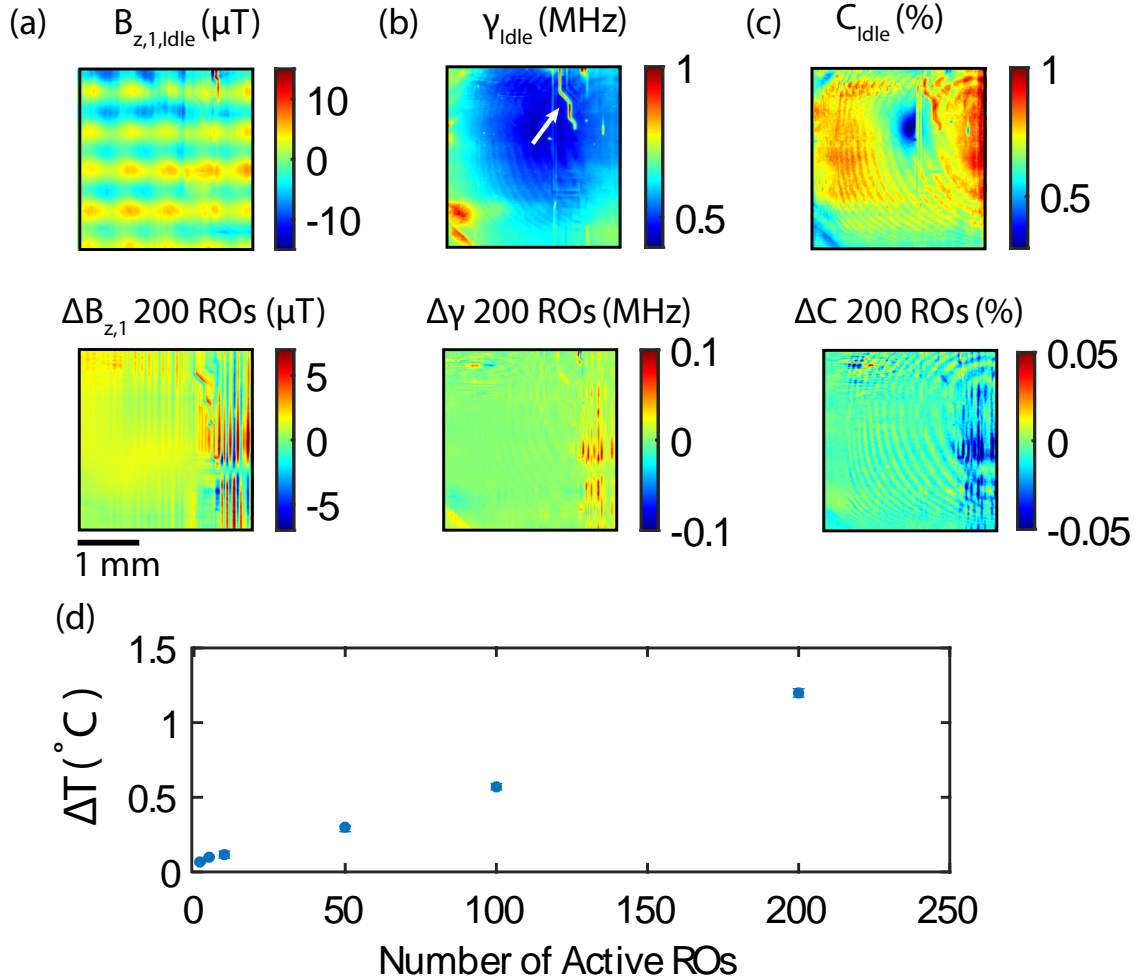
The center frequencies of the measured ODMR resonance features are determined by fitting the spectra with Lorentzian curves. The relevant measurement parameter for magnetometry is the Lorentzian line center, denoted x_0 , which is extracted by fitting the data with a Lorentzian function given by [S5]:

$$F = 1 + F_0 + \frac{C_1 \gamma^2}{(x - x_0 + A)^2 + \gamma^2} + \frac{C_2 \gamma^2}{(x - x_0)^2 + \gamma^2} + \frac{C_3 \gamma^2}{(x - x_0 - A)^2 + \gamma^2} \quad (S5)$$

where F_0 is an offset, C_1 , C_2 , and C_3 are the contrast values for the different hyperfine features of a given resonance, γ is the resonance linewidth, x_0 is the line center, and A is the hyperfine splitting treated as a constant 2.158 MHz. This fit is performed for each of the 8 (4 crystal axes and 2 electronic transitions) different resonance groupings. The contrast is treated as three different parameters for the three hyperfine features to account for differences due to extra small peaks from the forbidden hyperfine transitions [S6]. The resonances are sufficiently broadened by the MW power and high [N] of the diamond to allow for the linewidth to be treated as one parameter [S5].

D. Multimodal Imaging: Magnetic Field, Contrast, Linewidth, and Temperature

The main text presents DC magnetic field maps of active FPGAs that are determined from the measured magnetic field-induced splitting of NV ODMR resonance line centers. Determining the value of the resonance line centers requires fitting Lorentzian functions to the measured ODMR resonance features as described in the previous section. An example of the B_z field image determined from fitting to the measured ODMR spectra in each camera pixel is shown in Figure S1(a). Fitting also extracts the Lorentzian linewidth and contrast [S7], which contain useful information about the properties of magnetic fields emanating from the circuit, and in future work can be used as additional inputs to machine learning models to fingerprint IC activity.



Supplemental Figure S1. QDM images of activity (idle and 200 ROs in Region 1) from the decapsulated FPGA, based on various parameters emerging from the Lorentzian fit to NV ODMR spectra. (a) Images of the projection of magnetic field onto NV axis one. (b) Resonance linewidth images show a strong dependence on other features like MW power, laser power, strain gradients, time varying magnetic fields, and temporal variations that are fast relative to the measurement time. (c) Resonance contrast images contain similar information to the linewidth, but are strongly influenced by variations in the laser over the field-of-view. (d) Change in the average state dependent temperature is shown as a function of the number of active ring oscillators in Region 1 (regions are defined in the main text).

The activity state-dependent linewidth is dependent on several physical phenomena including magnetic field and strain gradients within a pixel, variations in the magnetic field over the measurement time, and spatial variations in the laser, microwaves, and bias field. Figure S1(b) shows an example of the calculated linewidth images for the idle and 200 RO active states. As indicated by a white arrow in Figure S1(b), one can see the effect of a strong broadening mechanism, which is likely due to strong zero-mean time varying magnetic fields (since this feature does not appear in the magnetic field map in S1(a)). Similar types of features can be seen in the Lorentzian contrast

89 images of the idle and 200 RO state in Figure S1(c). However, due to the strong dependence of the contrast on
 90 optical power [S7] these maps are more sensitive to interference fringes. These fringes are likely due to reflections of
 91 the green laser from the passivation layer of the decapsulated chip.

92 Temperature changes in the diamond are determined from common mode shifts of NV resonance line centers.
 93 The common mode shift for each pixel is calculated and then all the pixels are averaged together to give a single
 94 value for the bulk crystal temperature. The thermal conductivity of single crystal diamond is large enough that the
 95 diamond equilibrates to a uniform temperature on time scales much shorter than the measurement time. As such,
 96 wide field-of-view ensemble NV measurements in diamond are not well-matched for imaging temperature variations
 97 and are not suitable for determining regional activity on the IC based on thermal signatures. The changes in bulk
 98 crystal temperature can be used to improve state classification through understanding of power consumption in the
 99 chip, but do not allow for spatial selectivity.

100 In future work, the multimodal information from the magnetic field maps, linewidth, contrast, and temperature
 101 will be used to create a more detailed fingerprint of IC activity. These physical parameters provide a rich dataset of
 102 features that afford further dimensionality for characterization and classification.

103 E. Device Under Test Details

104 The die of the Artix-7 FPGA is covered by roughly 500 μm of epoxy resin packaging material, separating the
 105 diamond from the die for the intact configuration. This stand-off distance leads to smaller field amplitude at the NV
 106 sensor layer and acts as a low-pass filter decreasing the effective QDM spatial resolution of FPGA current sources
 107 [S8]. To bring the diamond closer to the die, one of the Artix-7 FPGAs is decapsulated (decapped) using a Nisene
 108 JetEtch Pro CuProtect decapsulator (Fig. 2(c) in the maint text). This process uses fuming sulfuric and nitric
 109 acid to remove the packaging material, exposing the die while leaving the FPGA electrically functional, including
 110 preservation of the copper wirebonds.

111 The structure of the wire-bonded Artix 7 die, shown in Fig. (d) in the main text, is optimal for studies of patterns
 112 of power delivery within the top metal layers of the FPGA. The thickest layers of the metal stack are usually closest
 113 to the top side of the package in wirebonded chips. These thick layers are used for power distribution due to their
 114 relatively low resistance characteristics compared to the other layers of the integrated circuit. Clock distribution
 115 networks and inputs/outputs (I/Os) occupy the next thickest layers, and data signals are in the lowest and thinnest
 116 metal layers. Prominent magnetic fields from the current densities in the power distribution network are therefore
 117 most easily detected with topside access of a wirebonded device. Magnetic field patterns from the lower-level data
 118 signals are likely not distinguishable with the present measurements. Note that Fig. 2(d) in the main text reveals
 119 large wire interconnects in the package substrate connecting the wirebonds and solder balls. These wires are deeper
 120 in the chip and are likely observable as low spatial frequency components in the magnetic field. As will be seen
 121 below, static fields from solder balls and other magnetic materials are also observable with the QDM; but can be
 122 distinguished from functional current flow by differential ring oscillator measurements.

123 F. State Dependent Current Delivery to Development Board

124 The global DC current delivered to the Nexys A7 development board is measured as a function of the number
 125 of active ROs to obtain an approximation of the current required by the FPGA for each state. The current was
 126 determined by measuring the voltage across a fixed resistance at the input of the development board. The time
 127 variation of the voltage was recorded on a fast (1 GHz) oscilloscope.

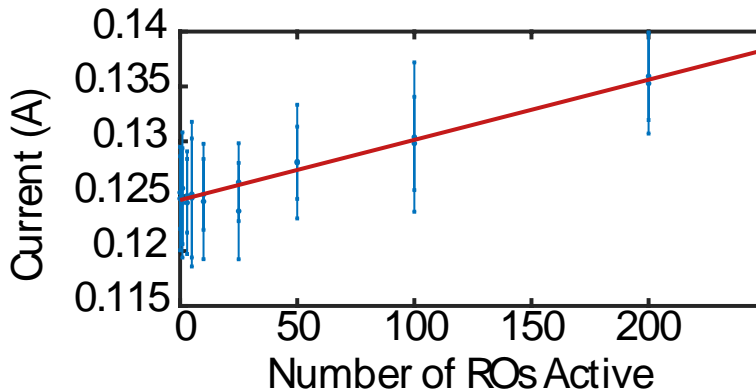
128 The Nexys A7 contains many components in addition to the Artix 7 FPGA and has many processes running in
 129 parallel to the FPGA. The measured voltage is consequently dependent on other processes executing on the board
 130 that are independent of the FPGA activity. This results in a voltage signal full of extraneous spikes and other
 131 information, degrading confidence in the measurement of DC currents (see Fig. S2). The voltage was measured on
 132 the scope for 1 ms at a sampling rate of 1 GHz. The current was calculated through precise measurement of the
 133 resistance used.

134 This process was repeated twice for each FPGA activity state, with ROs activated in Region 1. The resulting
 135 data is plotted in Figure S2. The error bars represent the standard deviation of the voltage over the 1 ms of signal
 136 acquisition. The current scales linearly with the number of ROs (0.055(6) mA per active RO) see Fig S2 The resultant
 137 linear fit is shown below.

$$I_{tot} = 0.055(6)(\text{mA}/\text{RO})N_{RO} + 125(4)\text{mA} \quad (\text{S6})$$

138 Assuming a simple model of the current being confined to a single wire-like structure and a stand-off distance of
 139 $\sim 15\mu\text{m}$ yields approximate scaling of 500 nT/RO. This is likely an over-estimate because the currents are distributed

140 over many wires and there can additionally be cancellation from neighboring sources. The activity state dependent
 141 current measured at the input are not necessarily exactly representative of the state dependent current on the die
 142 due to the complexity of components on the development board interfacing between the FPGA and the external
 143 power supply. However, these measurements are useful for informing general trends of current consumption of the
 144 FPGA.



Supplemental Figure S2. Plot of the measured DC current delivered to the development board as a function of the number of ROs active in Region 1 of the FPGA. The large error bars result from the activity of other components on the development board, independent from the FPGA, that draw varying amounts of current over the duration of a given measurement.

145

G. Measured Noise Floor

146 Properly calibrated and corrected measurements of a quiet subregion of the FPGA should result in a uniform
 147 magnetic field in all the pixels of the subregion. Any variation in the measured magnetic field across these pixels is
 148 a result of noise such as technical noise or more fundamental noise sources like shot noise. The dashed line in Figure
 149 S3(a) indicates one such low-activity subregion that is selected to exclude spatial current source variations of the idle
 150 state. The spatial noise floor is defined as the full-width-at-half-maximum of the histogram of magnetic field values
 151 of all the pixels in the subregion. Measurements over multiple experimental runs are averaged together to determine
 152 the magnetic field in each pixel. The histogram is plotted multiple times for a variable number of averaged runs. As
 153 the number of averaged runs increases, the width of the histogram narrows, demonstrating the suppression of noise
 154 with averaging over many runs.

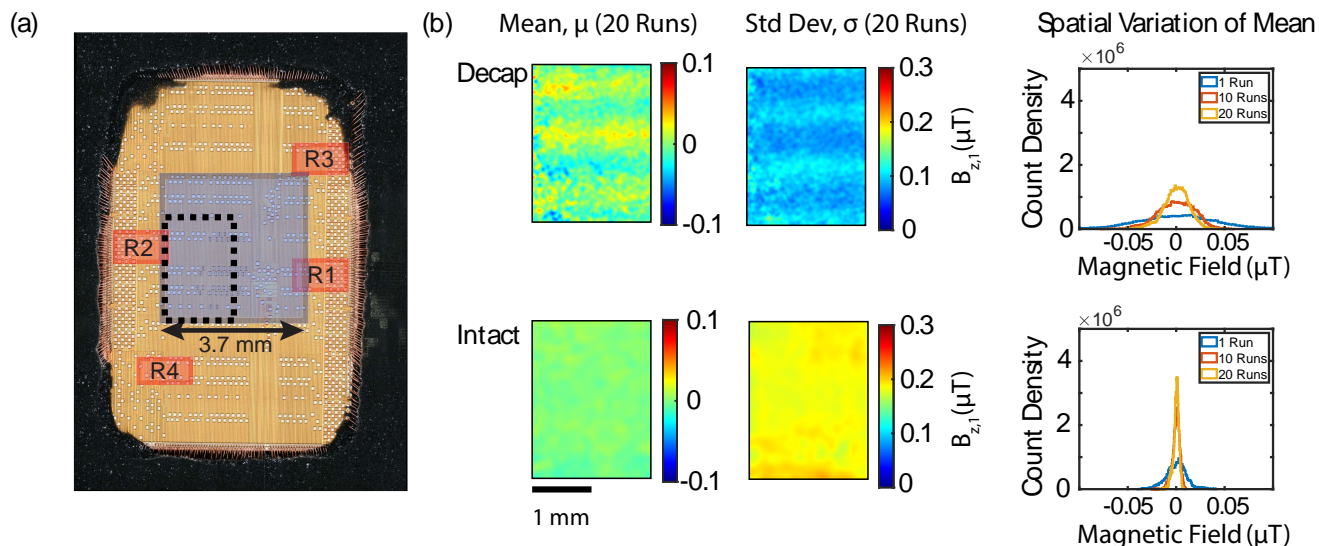
155 The spatial noise floor is thus an important figure-of-merit for characterizing QDM performance when measuring
 156 spatially varying, quasi-static magnetic fields. Twenty different data collection runs were utilized for this analysis.
 157 The mean and standard deviation for each pixel over these 20 measurements were calculated and plotted over the
 158 subsection field-of-view in Figure S3(b). The scaling of the noise floor as a function of number of runs for this dataset
 159 is indicated by a plotted histogram of the mean pixels after 1, 10, and 20 data collection runs. The high frequency
 160 spatial variation in the decapsulated (decap) data leads to a broader distribution of mean values. In contrast, the
 161 larger stand-off distance of the intact data allowed for more aggressive binning and Gaussian filtering to be utilized.
 162 This binning and filtering resulted in a lower noise floor for the intact data (2 nT) compared to the decap data (20
 163 nT). This noise floor is likely due to a combination of photon shot noise, laser intensity noise, and/or electronic noise
 164 from the camera.

165

H. Measurement Duration and Sensitivity

166 The duration of a given measurement is important for practical applications of the QDM and can limit feasibility
 167 of collecting large datasets needed for training more advanced machine learning models. A more detailed discussion
 168 on factors impacting measurement duration and bandwidth is given in Ref. [S9].

169 Total measurement time is the net result of multiple factors including the camera exposure time, the number of
 170 camera frames averaged together per microwave (MW) frequency, the number of MW frequencies monitored, and the
 171 associated data transfer and processing time. The measurements presented in the paper have an exposure time of ~ 4
 172 ms, which is sufficient to nearly saturate the pixel wells of the camera. Full-sensor readout, defined as using all camera



Supplemental Figure S3. (a) Dashed line indicates subset of pixels used for calculation of mean and standard deviation of QDM performance when measuring spatially varying, quasi-static magnetic fields. This region of the FPGA is relatively quiet while in the 0 RO/Idle State. (b) Mean and standard deviation of QDM imaged magnetic fields averaged over 20 runs, and the noise floor achieved in the mean data as a function of number of runs averaged together. Width of the histogram gives the noise floor: ~ 20 nT for the Decap dataset measurements and ~ 2 nT for the Intact dataset.

173 pixels, is used to measure the wide field-of-view while maintaining high spatial resolution. The full-sensor readout
 174 from the specific camera used in this study is about 6 ms and limits the fastest effective frame rate. Furthermore,
 175 this fixed readout time prevents the ability to increase the speed of measurements through decreasing the exposure
 176 time. Laser intensity variation over the duration of a measurement is generally a significant source of noise and each
 177 frame with MWs on is followed by a frame with MWs off to correct for this, doubling the time required for collecting
 178 data.

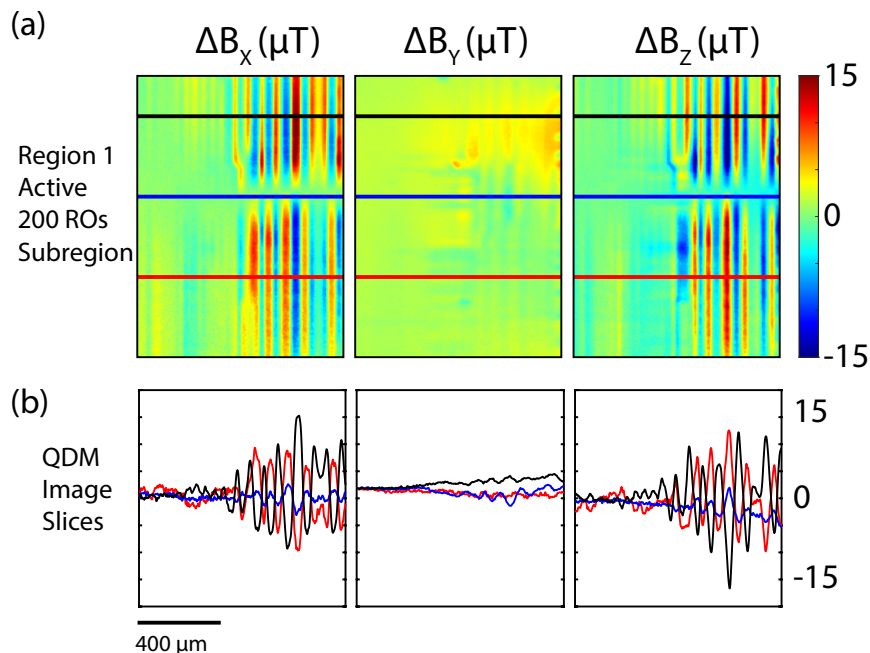
179 Measuring the ODMR spectrum over many MW frequencies improves the fidelity of fitting to determine the
 180 magnetic field, and ameliorates large perturbations in the magnetic bias field, diamond strain, and temperature.
 181 Measuring many frequencies per ODMR resonance also minimizes linewidth and contrast variations from influencing
 182 the magnetic field reconstruction. Typically, 60-80 MW frequencies are swept to sample a span of approximately 10
 183 MHz for each ODMR resonance. The sweep covers 2 resonances for the single-axis measurements and 8 resonances
 184 for the 4-axis vector measurements. The ODMR spectrum is measured multiple times until the averaged spectrum of
 185 a single pixel has a signal to noise ratio of >10 . For the single axis measurements this usually requires a measurement
 186 time of 5 minutes and for the 4-axis vector measurements this requires 20-30 minutes. Every measurement results
 187 in an ODMR spectrum for each of the $\sim 1200 \times 1200$ camera pixels. Given the measured noise floor of ~ 20 nT
 188 for 20 measurements, a 5 minute duration per measurement gives an approximate volume normalized sensitivity of
 189 $5 \mu\text{T} \mu\text{m}^{3/2} \text{Hz}^{-1/2}$ for all the pixels in the field-of-view. This experiment is optimized for a high dynamic range with
 190 high fit fidelity over a large field-of-view for thousands of measurements, motivating slower, more robust techniques to
 191 determine the FPGA state dependent magnetic fields. To compare with scanning techniques, the resulting effective
 192 measurement scan speed is $200 \mu\text{s}$ per pixel.

193 The required measurement duration can be decreased by using a low magnification, high NA objective [S10] to
 194 allow for the acquisition of a large field-of-view with much higher photon collection efficiency [S11]. To take advantage
 195 of this larger photon flux, a camera is needed that can handle the increased photon rate [S9, S12]. Furthermore,
 196 fewer MW frequencies can be monitored to optimally sample the ODMR spectra [S13, S14], thereby minimizing the
 197 time spent sweeping MW frequencies. Measurements can be further sped up by decreasing the field-of-view; allowing
 198 for the excitation laser to be focused onto a smaller area, enabling the use of a higher magnification objective,
 199 and requiring readout from a fewer number of pixels. Further optimization is needed to achieve $\sim\text{kHz}$ scale QDM
 200 magnetic imaging over mm fields of view.

201

I. Magnetic Field Image Slices

202 Line plots of the magnetic field are shown in Fig. S4 to elucidate features associated with a subset of the magnetic
 203 field images in Figure 3a of the main text. Specifically, data for the magnetic field magnitude of each vector
 204 component is plotted along line cuts taken above, below, and at the location of the ring oscillators. The sign change
 205 of the magnetic field is easily observable above and below the ring oscillators for the ΔB_X and ΔB_Z image slices.



Supplemental Figure S4. QDM vector magnetic field images of the decapsulated FPGA, a subset of images from Figure 3a in the main text for the decapped FPGA. (a) State dependent vector field images for 200 ROs active in Region 1. (b) Slices (line cuts) of the vector magnetic field images from (a). Black, red, and blue lines in (b) correspond to slices in (a) and are located above, below, and at the location of ring oscillator region R1, respectively.

206

J. Vector Magnetic Field Measurements of Additional Active Regions

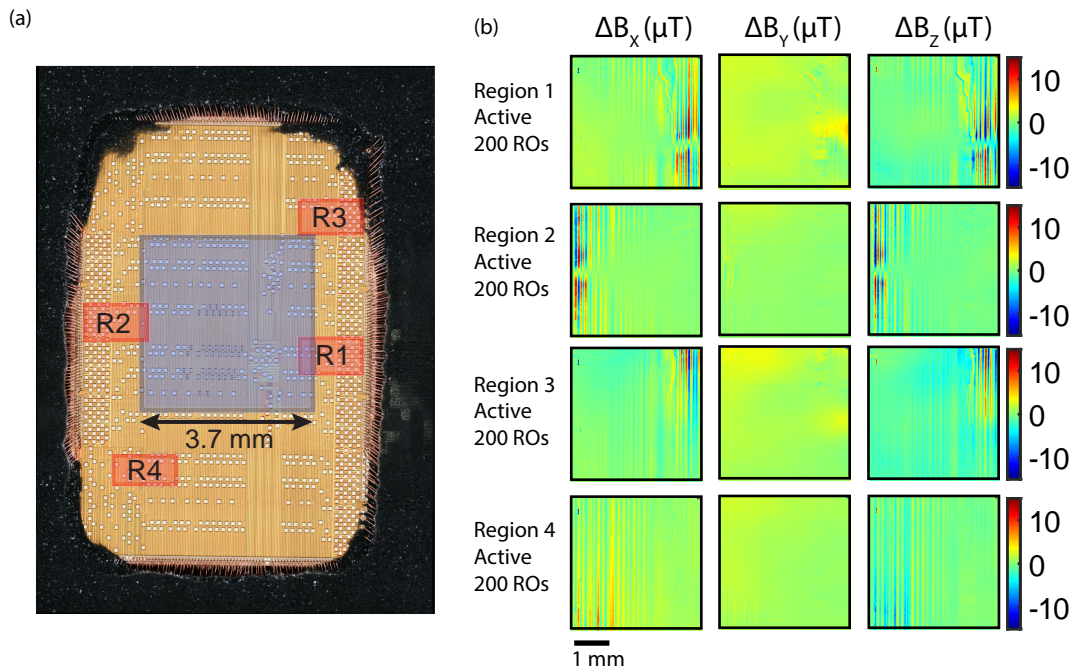
207 The decapsulated FPGA was programmed to have clusters of ROs activated in four distinct location-locked regions
 208 as shown in Figure S5(a). ROs were active in only one region at any time. The main text discusses two regions,
 209 R1 and R2, that were within the QDM field-of-view. The other two regions, R3 and R4, were outside of the QDM
 210 field-of-view, and were activated to search for extended indicators of regional activity.

211 Figure S5(b) shows that activity state-dependent magnetic fields are evident for 200 ROs in R3 and R4, even
 212 though both regions are outside the measurement field-of-view. Figure S5(b) also reproduces the fields for 200 ROs
 213 in R1 and R2 presented in Figure 3 of the main text for comparison. These measurements take advantage of the
 214 extended current routing networks on the chip. One can start to infer some general trends about shared resources on
 215 the FPGA. For example, activation of 200 ROs in R1 and R3, both on the right side of the die, gives rise to strong
 216 ΔB_Y fields in similar locations in the field-of-view.

217

K. Larger Measurement Stand-off Distance Using a 40 micron NV Layer

218 An additional 5 mm \times 5 mm \times 0.5 mm diamond was used in the QDM to probe an intermediate stand-off
 219 measurement distance for both the decapsulated and intact FPGAs. This diamond had a 40 μm surface layer of NV
 220 centers consisting of [^{12}C] \sim 99.95%, [^{15}N] \sim 10 ppm, and [NV] \sim 1 ppm. The diamond was placed directly on the
 221 FPGA with the NV layer in contact with the FPGA surface. The thicker NV layer gives rise to a larger effective



Supplemental Figure S5. QDM vector magnetic field images of decapsulated FPGA (a) Location of the active RO regions (red boxes) relative to the QDM field-of-view (grey box). (b) Spatial fingerprint of vector magnetic field maps for ROs active in each of the four different regions.

stand-off distance because the average NV within the ensemble is farther away from the magnetic field source. The resulting magnetic field maps, shown in Figure S6, have coarser spatial resolution for the decapsulated measurements due to the larger stand-off distance. Consequently, the subtle features seen in data presented in the main text are no longer evident.

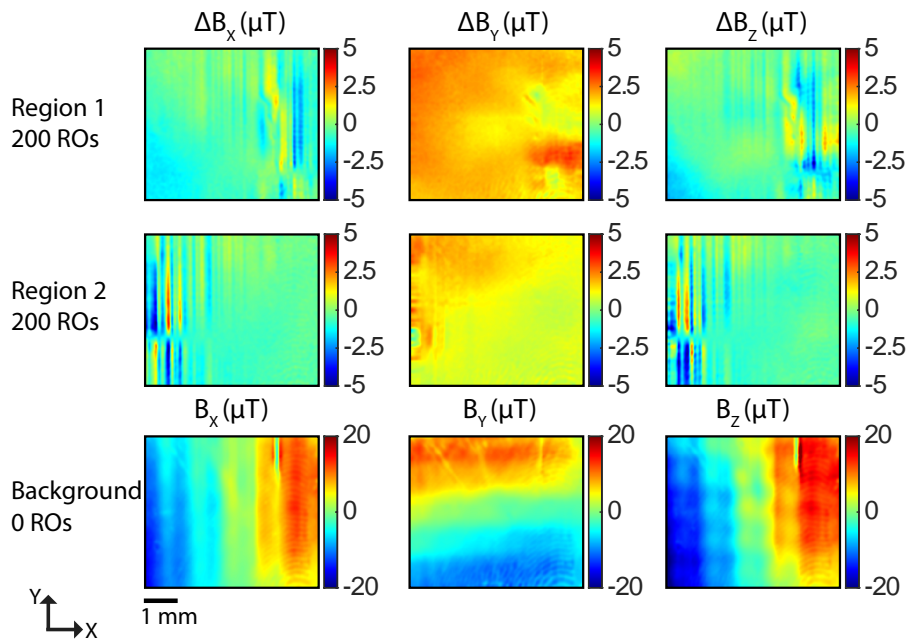
Despite the lower resolution, such a diamond could be advantageous for the optimization of measuring intact ICs where the higher spatial frequencies are already suppressed by the large stand-off distance caused by the package. Also, a thicker NV layer will improve magnetic field sensitivity due to the larger number of total NVs contributing to the signal. Another feature of this diamond that can prove advantageous for future measurements is the larger, 5 mm × 5 mm area of the diamond. These larger dimensions allow for a wider field-of-view showing, more of the activity from R1 and R2 simultaneously, as shown in Figure S6 in comparison to the figures in the main text.

L. COMSOL Simulations

The stand-off distance between the NV measurement plane and the magnetic field sources impacts the measurement sensitivity and spatial resolution. The FPGA contains multiple layers of interconnects: eleven metal layers in the silicon die and additional metal layers in the package of the FPGA that connect the bond wires to the ball grid array. These structures are visible in the SEM images of the FPGA cross section shown in Figure 2 of the main text. The metal layers in the silicon die have micron to sub-micron length scales, whereas the package interconnects have 10-100 μm length scales.

The current densities in these metal layers act as sources of the measured magnetic fields. The stand-off distance of the NV layer and the sources determines which metal layer contributions dominate. The NV layer was within ~ 5-10 μm of the top metal layer of the die and within 300 μm of the package interconnects for the decapsulated chip. The resulting field measurements were dominated by the close, top metal layer. The resin-epoxy layer of the intact chip increased the stand-off distance of the NV plane to 500 μm from the top metal layer and 800 μm from the package interconnects. The resulting field measurements for the intact chip were dominated by the large and distant package interconnects.

This near- and far-field behavior of static magnetic fields is demonstrated using finite element analysis modeling with the commercial finite element software COMSOL 5.4 (Comsol, Inc.). The model geometry, depicted in Figure



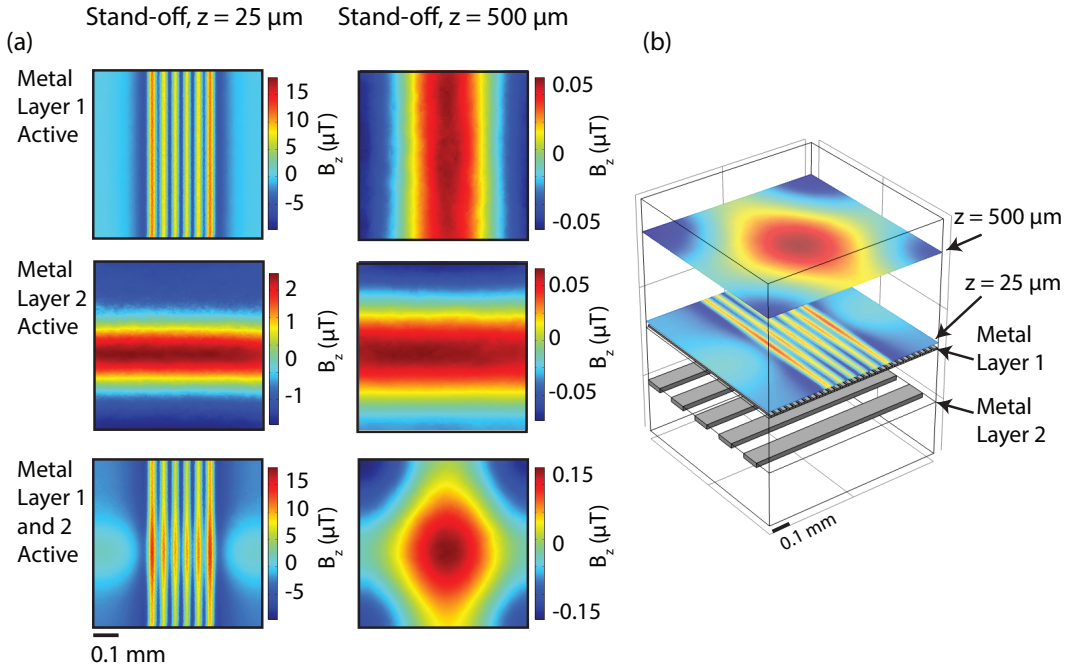
Supplemental Figure S6. A diamond with a thicker NV layer was used to take the same vector magnetic field measurements presented in Figure 3 of the main text for the decapsulated FPGA. The thicker NV layer results in a larger effective measurement stand-off distance, resulting in lower resolution images of the spatial variation of the magnetic field.

248 **S7**, includes the $21.6 \mu\text{m}$ wide wires of the top metal layer with $12.6 \mu\text{m}$ inter-wire spacing and the $100 \mu\text{m}$ wide
 249 wires of the package interconnects with $100 \mu\text{m}$ inter-wire spacing. The two layers are defined in the X - Y plane and
 250 are separated in Z by the $300 \mu\text{m}$ of the silicon die. The governing magnetostatic equation $\vec{\nabla} \times \mathbf{H} = \mathbf{J}$ is solved for
 251 the model geometry with $\mu\mathbf{H} = \mathbf{B}$, with a magnetic insulation boundary condition, $\mathbf{n} \times \mathbf{A} = 0$ for $\mathbf{B} = \vec{\nabla} \times \mathbf{A}$, and a
 252 current of $\sim 10 \text{ mA}$ applied with reverse bias on a subset of adjacent wires in each layer. The current magnitude was
 253 chosen to be similar to the measured current drawn by the board with 200 ROs active on the FPGA. A tetrahedral
 254 mesh was used consisting of elements half the size of the $12.6 \mu\text{m}$ wire spacing in the vicinity of the top metal layer,
 255 and scaled up for regions of the computational domain far away from the wires.

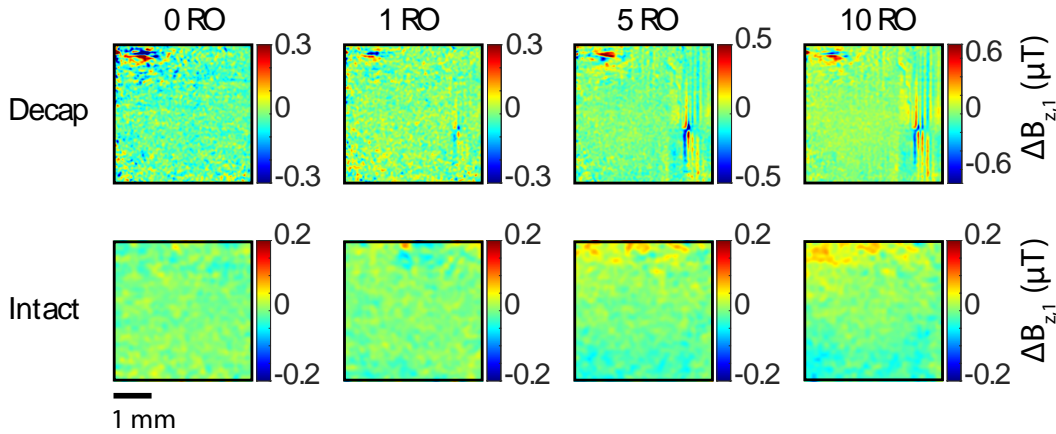
256 The magnetic inductance \mathbf{B} is solved for everywhere in the domain using COMSOL's Magnetic Fields (mf) module.
 257 The calculation is completed in two stages: the current density in the wire domains is initially solved for using the
 258 applied current condition and the electrical conductivity of the wires, $\sigma = 6e7 \text{ S/m}$; the current density is then used
 259 as the source term to determine the magnetostatic fields. Figure **S7** plots the resulting magnetic fields for three cases:
 260 (i) a current bias applied to the wires in both metal layers, (ii) a current bias applied to wires in only the top metal
 261 layer, (iii) a current bias applied only to wires in the package (bottom) layer. The resulting X - Y magnetic fields for
 262 each case are plotted at two Z stand-off distances, $25 \mu\text{m}$ and $500 \mu\text{m}$, corresponding to the decapsulated and intact
 263 chip measurement configurations respectively. For the case of current applied to both metal layers, the magnetic
 264 fields from the small wires of the top metal layer are seen to dominate for the measurement plane with small stand-off
 265 distance, whereas the magnetic fields from the wires of the bottom interconnect layer are seen to dominate for the
 266 large stand-off distance. This is consistent with our interpretation of the NV measurements presented in the main
 267 text.
 268

269 M. Data for Low Number Active RO States

270 Representative QDM images taken from a series of measurements for single acquisitions of low numbers of ROs are
 271 given in Figure **S8** for decapsulated and intact chips. Long term drift and large background fields are corrected for
 272 by subtracting off the nearest idle (0 RO) state in the measurement series. The measured states of the decapsulated
 273 chip are relatively easy to classify by visual inspection, consistent with the perfect accuracy in classification presented
 274 in the main text. The differences between states are more subtle in the intact data for low number of active ROs.
 275 The high classification accuracy (80%) achieved in the main text for these states illustrates the value of the machine
 276 learning classifier.



Supplemental Figure S7. (a) COMSOL Simulations of magnetic fields from a configuration of two layers of metal wires representing the small top metal layer (denoted metal layer 1) of the FPGA die and the large interconnect wires (denoted metal layer 2) of the package. The simulations reveal that different features have an importance that is weighted by the stand-off distance. Small, nearby sources dominate with small stand-off distance, and large, far away sources dominate with large stand-off distance. (b) 3D visualization of the measurement planes relative to the position of the current sources.

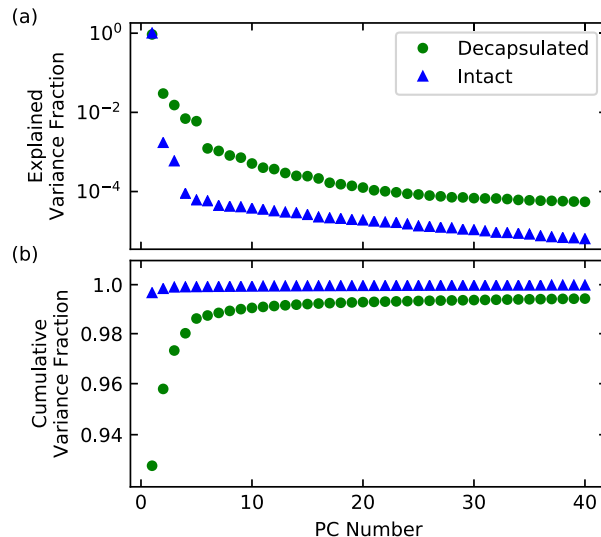


Supplemental Figure S8. Representative QDM images of single runs of activity states with small numbers of RO that are used as inputs for the machine learning classification. The differences in the decapsulated chip states are observable through inspection, but the intact chip state differences are more subtle.

277

N. Explained Variance of Principal Components

278 Principal component analysis (PCA) is used as a dimensionality reduction tool to convert magnetic field images
 279 to a subset of projections (scores) along the first several principal components (PCs). These PCs are determined
 280 by sequentially finding axes that explain the most variance in a high-dimensional dataset such that these axes are
 281 orthogonal. Typically only a small number of scores are needed to describe a given instantiation of the dataset.



Supplemental Figure S9. (a) The fraction of variance explained by the n^{th} principal component (PC) in the decapsulated dataset (green dots) and the intact dataset (blue triangles). (b) The cumulative fraction of variance explained by the first n PCs as a function of n (colors and markers are same as above). For both datasets, $> 99\%$ of the variance is explained by the first 9 PCs.

Subsequent scores will only contain information about the noise in the data.

Figure S9(a) shows the fraction of variance explained by the n^{th} PC in both the decapsulated and intact datasets for the first 40 PCs. The first PC explains nearly all the variance in the magnetic field images, after which the explained variance drops off rapidly, ultimately depending only on noise and other RO state-independent information. Figure S9(b) shows the cumulative variance fraction for the first n PCs as a function of n . For the intact dataset, the first PC alone accounts for $> 99\%$ of the variance in the magnetic field images. For the decapsulated dataset, the first $n = 9$ PCs account for $> 99\%$ of the variance. The first $n = 9$ PC scores for each image are therefore used to capture all of the non-noise based information. These 9 scores are used to train the SVM classifier.

O. Relative Importance of Each Principal Component

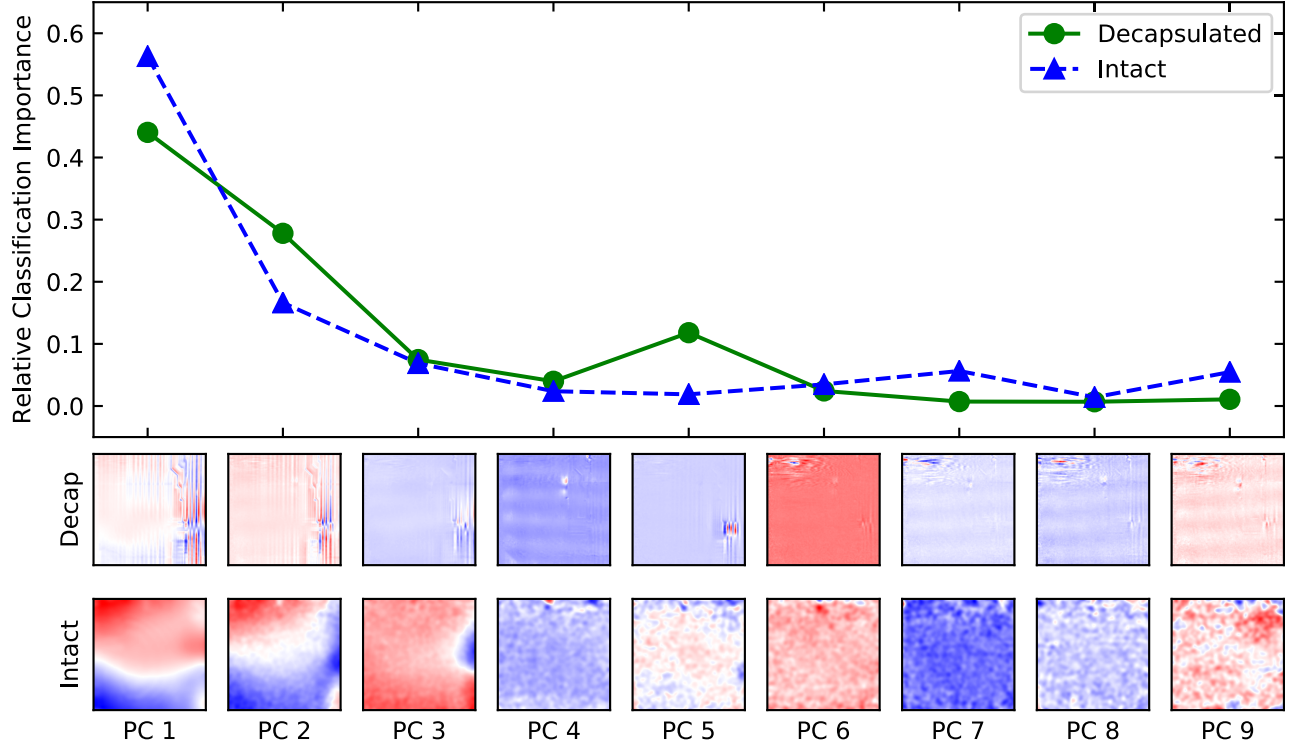
Figure S10 shows all of the first 9 PCs used in the chip state classification for both the decapsulated and intact datasets. A relative classification importance (defined below) is also calculated for each PC. The first two PCs of both datasets most strongly resemble the magnetic field images. As such, these PCs can naively be assumed to be the most useful for state classification, which agrees with these PCs having the highest importance factor. Additional PCs that visually capture state-independent information accordingly have low importance. For example, PC 4 in the decapsulated dataset nicely captures the solder balls present in all magnetic field images, and PCs 6 through 9 capture activity in the upper left corner that is also present in all images.

In the intact dataset, PCs 4 through 9 appear noisy; however, PCs 7 and 9 both have a slightly elevated importance. The source of this importance is unknown, but given the small fields produced by the ROs on top of a larger background field, it is not surprising that PCs explaining a smaller fraction of data variance carry a higher importance in classification. The overall trend of decreasing importance with PC further strengthens the assertion that 9 PC scores suffice to classify each dataset.

The definition of the relative classification importance requires details of a linear support vector machine (SVM) classifier. As described in the main text, linear SVMs seek to create a boundary between two classes, $y \in \{-1, 1\}$, of an N dimensional dataset by finding the $N - 1$ dimensional hyperplane that maximizes the orthogonal distance from both classes. Any hyperplane is defined by its normal vector and a constant offset. For the optimal hyperplane boundary defined by the SVM classifier, we denote its normal vector as \mathbf{w} and its constant offset as b . Any point, \mathbf{x} , lying in this hyperplane will satisfy the equation

$$\mathbf{w} \cdot \mathbf{x} - b = 0 \quad (\text{S7})$$

The SVM classification, y' , of an arbitrary point, \mathbf{x}' , will then be determined by whether this point lies above or



Supplemental Figure S10. The relative importance for support vector machine (SVM) classification of each of the 9 principal components (PCs) used in both the decapsulated and intact datasets. The PCs that contain the most state dependent information have the most importance. Conversely, the PCs containing state independent information have the least importance.

310 below this plane, written mathematically as

$$y'(\mathbf{x}') = \text{sgn}(\mathbf{w} \cdot \mathbf{x}' - b) \quad (\text{S8})$$

311 We can interpret the normal vector, \mathbf{w} , as a weighting vector for each dimension in the N dimensional space and
 312 thus define a relative classification importance, I_j , of the j^{th} dimension as

$$I_j = \frac{|w_j|}{\sum_{j=1}^N |w_j|} \quad (\text{S9})$$

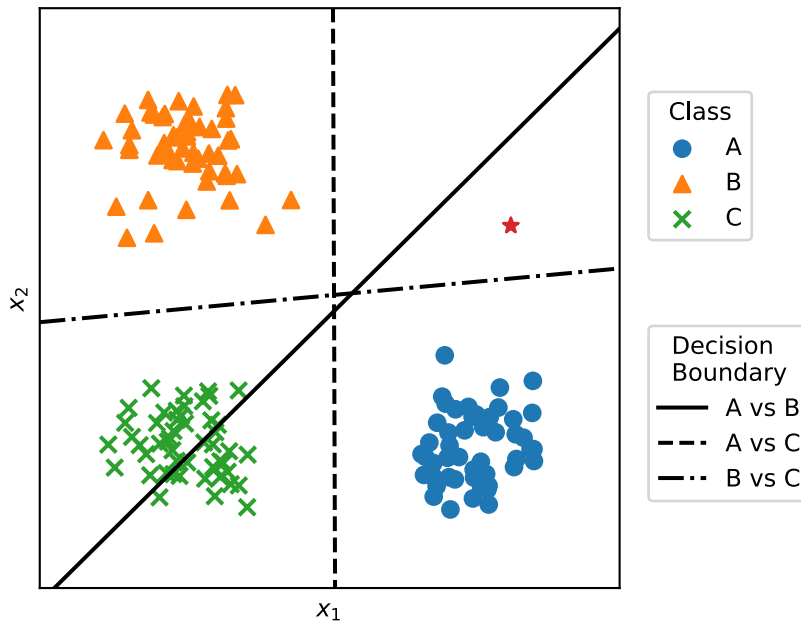
313 In the case of M classes (where $M > 2$), a one-versus-one classification scheme is implemented, whereby each class
 314 is compared with every other class. This yields $K = \frac{1}{2}M(M - 1)$ hyperplane boundaries, each with a normal vector,
 315 \mathbf{w}_k , and a constant, b_k , for $k = 1, 2, \dots, K$. A simple pedagogical example (not used for QDM data analysis) with
 316 $N = 2$ dimensions (x_1 and x_2) and $M = 3$ classes (A, B, and C) is shown in Figure S11. $N = 2$ gives lines for the
 317 hyperplanes, and $M = 3$ gives $K = 3$ decision boundary lines. The red star represents a hypothetical new data point
 318 in need of classification. It will get classified as A twice and B once. The red star will consequently receive a final
 319 classification of A.

320 The relative classification importance of the j^{th} dimension for the k^{th} one-versus-one comparison is defined as

$$I_j^k = \frac{|w_{k,j}|}{\sum_{j=1}^N |w_{k,j}|} \quad (\text{S10})$$

321 The overall relative classification importance of the j^{th} dimension will then be given by

$$I_j = \frac{\sum_{k=1}^K I_j^k}{\sum_{j=1}^N \sum_{k=1}^K I_j^k} \quad (\text{S11})$$



Supplemental Figure S11. A simple SVM model (used only as a pedagogical example) with $N = 2$ dimensions (x_1 and x_2) and $M = 3$ classes (A, B, and C). Three lines represent the $K = 3$ hyperplane decision boundaries for each class comparison. The red star represents a new data point in need of classification. It will get two votes for A and one vote for B and thus will get a classification of A.

322

P. Additional PC Score Plots

In addition to the PC 1 score versus PC 2 score plot shown in the main text, Figure S12 shows all 10 pairs of scores for PCs 1 through 5 in both the decapsulated and intact datasets. The scores are normalized by the number of pixels in each image (different for the decapsulated and intact datasets) so as to give an idea of the contribution of each PC to the magnetic field images.

PCs that are useful in chip activity state classification are distinguishable from those that are not. For example, in the decapsulated dataset, PC 4 does not well separate differing numbers of ring oscillators (ROs), which is expected as it had the lowest importance factor of the first 5 PCs. Furthermore, PC 5 is useful in separating 1, 5, and 10 ROs, while PCs 1 and 2 are useful in separating 50, 100, and 200 ROs. In the intact dataset, PCs 1 and 2 are the most useful and PCs 4 and 5 are the least useful as expected from their high and low importance factors, respectively.

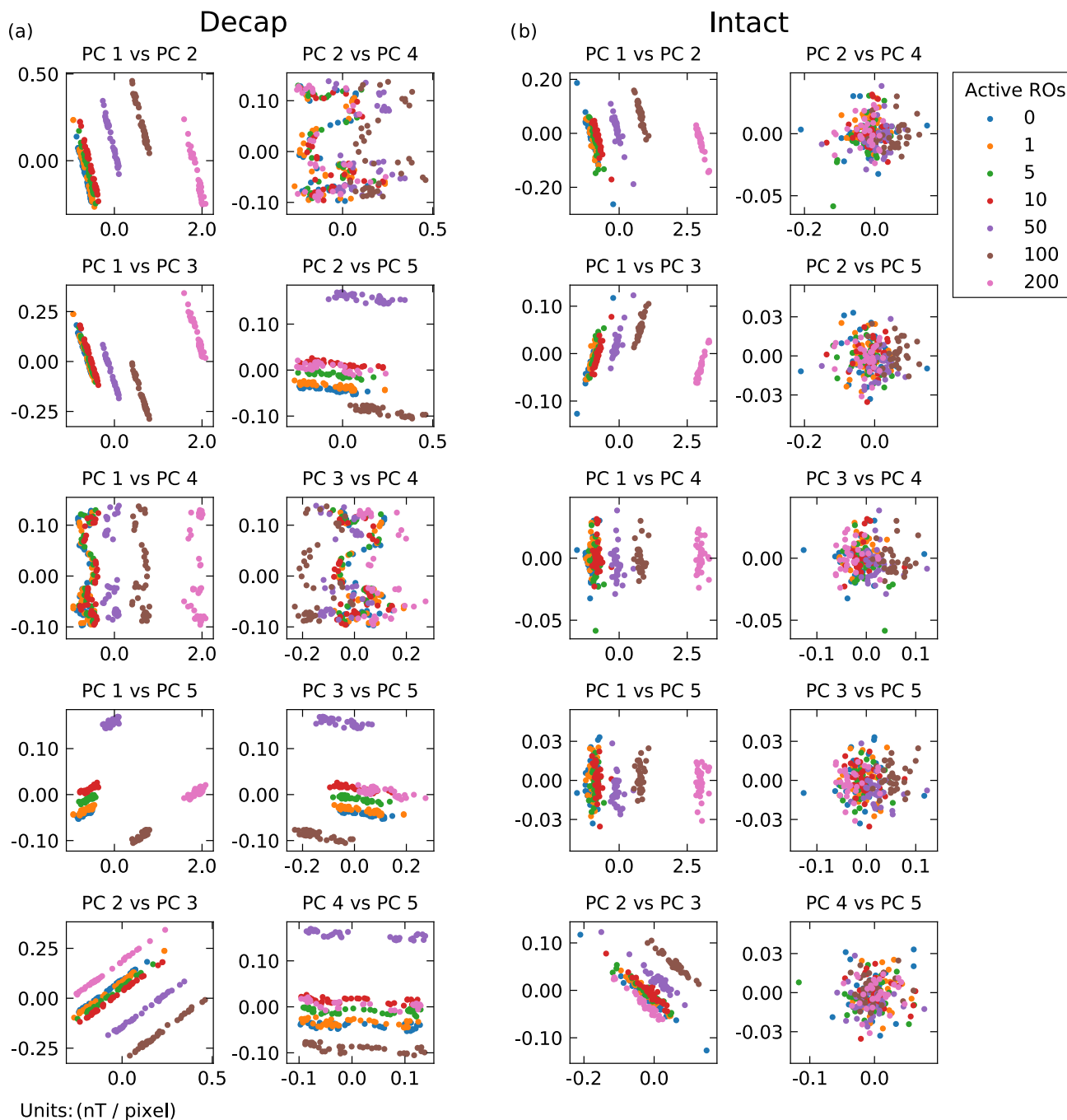
332

Q. Hyperparameter Cross Validation

When a training dataset contains outliers or is not linearly separable, the linear SVM classifier will struggle or even fail to find a hyperplane that will generalize well to predictions on the test set. To address this problem, implementations of SVM such as the `scikit-learn` class `svm.SVC()` used in this analysis will allow for some training samples to be misclassified in order to generalize well to the test set. The degree to which this is allowed is controlled by a regularization parameter, C . More precisely, a higher value of C attempts to correctly classify every training sample while a lower value of C will allow for more misclassifications of the training data. The regularization parameter thus represents a delicate balance between obtaining a good fit to the training set and generalizing well to the test set.

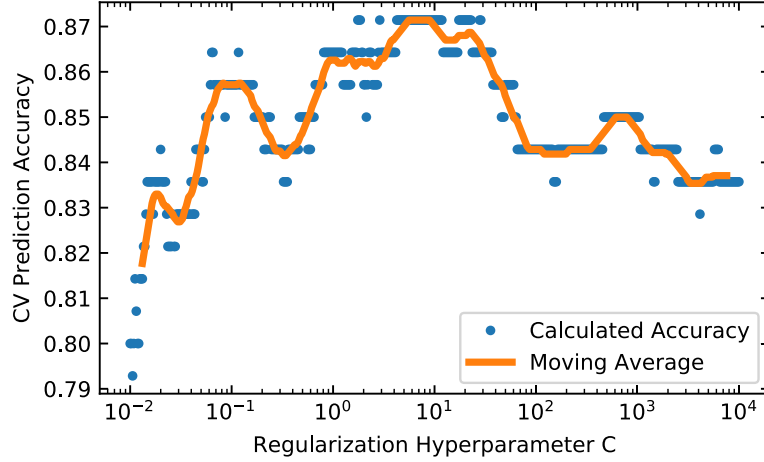
In order to determine the optimal value of C , we employ a 10-fold cross validation (CV) procedure. The training set is divided into 10 equal parts (folds). The first fold is used as a validation set and the remaining 9 folds are used as a new training set. A value of C is chosen and the PCA + SVM model is fit using the new training set. The model is then evaluated on the validation set and the accuracy is recorded. This process is repeated until each of the 10 folds have been used as the validation set. The CV accuracy for this value of C is then recorded as the average of the 10 validation accuracies. We repeat the entire process while varying C . Finally, we select the value of C that maximizes the CV accuracy and refit the model using all 10 folds as the training set. The test set containing as yet unseen data is then used to estimate the model accuracy by evaluating the final fitted model to this dataset.

348



Supplemental Figure S12. (a) Pairs of PC scores plotted against each other for PCs 1 through 5 in the decapsulated (decap) dataset. Units are nT / pixel and active number of ring oscillators (ROs) is color coded according to the legend. (b) The analogous plot for the intact dataset. Unlike the analogous plot in the main text, these plots are not on an equal aspect ratio and thus the slopes of groups of points carry less meaning.

349 The decapsulated dataset is easily separated by SVM and thus does not require CV of the regularization parameter.
 350 On the contrary, the intact dataset is not as easily separated and thus does require CV; figure S13 shows the results
 351 of this procedure. The discretization of the accuracies results from the relatively small training/validation sets (i.e.
 352 each jump in accuracy corresponds to one more correct prediction in the validation set). A 21 point moving average
 353 is included to smooth out the CV prediction accuracy. It is evident from this curve that the optimal value of C
 354 occurs at about $C = 6$ and hence this value is chosen for the final model in the intact dataset.



Supplemental Figure S13. Cross validation of the SVM regularization hyperparameter, C . A 21 point moving average is included to aid the eye. The optimal value is selected at $C = 6$.

R. Noise Propagation in PCA

A better intuition for the spread of datapoints in the PC score plots is obtained from looking at the impact of two simple sources of extraneous variation on the value of the PC score. These sources are spatially uniform offsets (for example, this well approximates drifts in the bias field) and Gaussian noise. As defined in the main text, the PC score is

$$S^{i,j} = \frac{1}{MN} \sum_{m=1}^M \sum_{n=1}^N W_{m,n}^i B_{m,n}^j \quad (\text{S12})$$

where each image is composed of $M \times N$ pixels, \mathbf{B}^j is the magnetic field image, and \mathbf{W}^i is the i 'th principal component.

A spatially uniform offset, Δ , is a constant value added to every pixel of an image, and can propagate through to the principal component analysis. The first two principal components of the decapsulated and intact chip analysis are used to explicitly determine the nature of Δ propagation through the PC analysis. The addition of Δ to a magnetic field image will result in an additional contribution, $\delta_{\Delta} S^{i,j}$, to the PC score giving

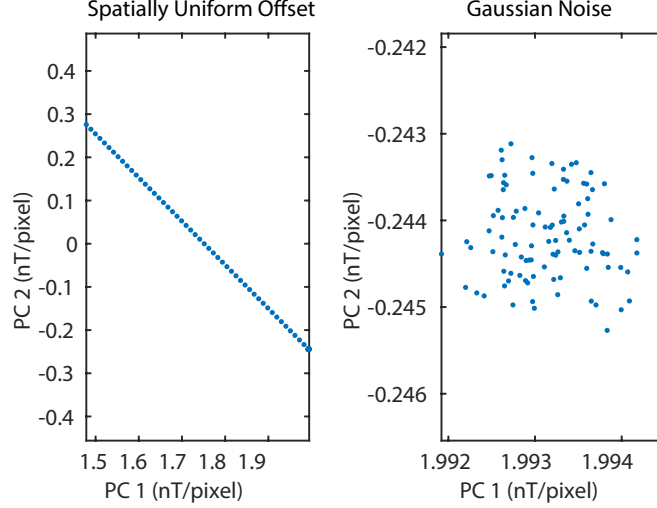
$$\begin{aligned} S^{i,j} + \delta_{\Delta} S^{i,j} &= \frac{1}{MN} \sum_{m=1}^M \sum_{n=1}^N W_{m,n}^i (B_{m,n}^j + \Delta) \\ &= \frac{1}{MN} \sum_{m=1}^M \sum_{n=1}^N W_{m,n}^i B_{m,n}^j + \frac{1}{MN} \sum_{m=1}^M \sum_{n=1}^N W_{m,n}^i \Delta \end{aligned} \quad (\text{S13})$$

The first term is just the original score, Eq. S12, for the magnetic field $B_{m,n}^j$, so $\delta_{\Delta} S^{i,j}$ can be solved for directly. Since Δ is a spatially uniform offset, it can be pulled out of the summation

$$\delta_{\Delta} S^{i,j} = \frac{\Delta}{MN} \sum_{m=1}^M \sum_{n=1}^N W_{m,n}^i \quad (\text{S14})$$

Each PC score will have a different value $\delta_{\Delta} S^{i,j}$ from the offset Δ due to the summation. The expected slope of the line for the PC2 versus PC1 plotted in Figure 5 of the main text is determined by $\delta_{\Delta} S_1 / \delta_{\Delta} S_2$; this ratio gives a slope of -0.99, consistent with the slope in the figure. Any spatially uniform variations for a given FPGA activity state between different images will fall on a line with this slope. For the intact dataset, the principal components are different and the expected slope of variation is $\delta_{\Delta} S_1 / \delta_{\Delta} S_2 \sim -3.03$, which is consistent with the Figure 5 in the main text.

The addition of spatial Gaussian noise ($X_{m,n}$) with zero mean and standard deviation α to a magnetic field image



Supplemental Figure S14. The impact of different noise sources on PCA, shown for an example of the QDM magnetic image for 200 ROs on the decapsulated chip. (a) A spatially uniform offset of 10 nT is added between each point along the line. (b) Gaussian noise with standard deviation of 100 nT is added. Note the dramatically different scales between the two plots.

will result in an additional contribution to the PC score giving

$$\begin{aligned}
 S^{i,j} + \delta_{\alpha X} S^{i,j} &= \frac{1}{MN} \sum_{m=1}^M \sum_{n=1}^N W_{m,n}^i (B_{m,n}^j + \alpha X_{m,n}) \\
 &= \frac{1}{MN} \sum_{m=1}^M \sum_{n=1}^N W_{m,n}^i B_{m,n}^j + \frac{1}{MN} \sum_{m=1}^M \sum_{n=1}^N W_{m,n}^i \alpha X_{m,n}
 \end{aligned} \tag{S15}$$

Similar to Eq. S14, the contribution due to Gaussian noise can be separated, yielding

$$\delta_{\alpha X} S^{i,j} = \frac{\alpha}{MN} \sum_{m=1}^M \sum_{n=1}^N W_{m,n}^i X_{m,n} \tag{S16}$$

The value and properties of this term depend on the precise spatial distribution of $W_{m,n}^i X_{m,n}$, so no general statement can be made on the impact of Gaussian noise. Figure S14 shows numerical simulations for these two different possible sources of variation, spatially uniform offsets and Gaussian noise. The plots confirm the general intuition from the results of the above derivations. In the specific case of PC1 and PC2 for the decapsulated and intact chips with $\alpha \approx \Delta$, one then has $\delta_{\Delta} S^{i,j} \gg \delta_{\alpha X} S^{i,j}$.

Further numerical simulations would be needed for other sources of variation including multiplicative noise, spatially varying offsets, etc., due to a strong dependence on the exact spatial features of the magnetic field images and principal component basis vectors.

-
- [S1] F Dolde, H Fedder, M W Doherty, T Nöbauer, F Rempp, G Balasubramanian, T Wolf, F Reinhard, L C L Hollenberg, F Jelezko, and J Wrachtrup. Electric-field sensing using single diamond spins. 2011.
- [S2] John F Barry, Jennifer M Schloss, Erik Bauch, Matthew J Turner, Connor A Hart, Linh M Pham, and Ronald L Walsworth. Sensitivity optimization for nv-diamond magnetometry. *arXiv preprint arXiv:1903.08176*, 2019.
- [S3] V. M. Acosta, E. Bauch, M. P. Ledbetter, A. Waxman, L.-S. Bouchard, and D. Budker. Temperature dependence of the nitrogen-vacancy magnetic resonance in diamond. *Phys. Rev. Lett.*, 104:070801, Feb 2010.

- 391 [S4] Erik Bauch, Connor A. Hart, Jennifer M. Schloss, Matthew J. Turner, John F. Barry, Pauli Kehayias, Swati Singh,
392 and Ronald L. Walsworth. Ultralong dephasing times in solid-state spin ensembles via quantum control. Phys. Rev. X,
393 8:031025, Jul 2018.
- 394 [S5] D. R. Glenn, R. R. Fu, P. Kehayias, D. Le Sage, E. A. Lima, B. P. Weiss, and R. L. Walsworth. Micrometer-scale
395 magnetic imaging of geological samples using a quantum diamond microscope. Geochemistry, Geophysics, Geosystems,
396 18(8):3254–3267, 2017.
- 397 [S6] Jennifer M. Schloss, John F. Barry, Matthew J. Turner, and Ronald L. Walsworth. Simultaneous broadband vector
398 magnetometry using solid-state spins. Phys. Rev. Applied, 10:034044, Sep 2018.
- 399 [S7] A. Dréau, M. Lesik, L. Rondin, P. Spinicelli, O. Arcizet, J.-F. Roch, and V. Jacques. Avoiding power broadening in
400 optically detected magnetic resonance of single nv defects for enhanced dc magnetic field sensitivity. Phys. Rev. B,
401 84:195204, Nov 2011.
- 402 [S8] Bradley J Roth, Nestor G Sepulveda, and John P Wikswo Jr. Using a magnetometer to image a two-dimensional current
403 distribution. Journal of applied physics, 65(1):361–372, 1989.
- 404 [S9] Edlyn V Levine, Matthew J Turner, Pauli Kehayias, Connor A Hart, Nicholas Langellier, Raisa Trubko, David R Glenn,
405 Roger R Fu, and Ronald L Walsworth. Principles and techniques of the quantum diamond microscope. Nanophotonics,
406 8(11):1945–1973, 2019.
- 407 [S10] Christopher A. Werley, Miao-Ping Chien, and Adam E. Cohen. Ultrawidefield microscope for high-speed fluorescence
408 imaging and targeted optogenetic stimulation. Biomed. Opt. Express, 8(12):5794–5813, Dec 2017.
- 409 [S11] D. Le Sage, L. M. Pham, N. Bar-Gill, C. Belthangady, M. D. Lukin, A. Yacoby, and R. L. Walsworth. Efficient photon
410 detection from color centers in a diamond optical waveguide. Phys. Rev. B, 85:121202, Mar 2012.
- 411 [S12] Adam M. Wojciechowski, Mürsel Karadas, Alexander Huck, Christian Osterkamp, Steffen Jankuhn, Jan Meijer, Fedor
412 Jelezko, and Ulrik L. Andersen. Contributed review: Camera-limits for wide-field magnetic resonance imaging with a
413 nitrogen-vacancy spin sensor. Review of Scientific Instruments, 89(3):031501, 2018.
- 414 [S13] John F. Barry, Matthew J. Turner, Jennifer M. Schloss, David R. Glenn, Yuyu Song, Mikhail D. Lukin, Hongkun
415 Park, and Ronald L. Walsworth. Optical magnetic detection of single-neuron action potentials using quantum defects
416 in diamond. Proceedings of the National Academy of Sciences, 2016.
- 417 [S14] Ilja Fescenko, Abdelghani Laraoui, Janis Smits, Nazanin Mosavian, Pauli Kehayias, Jong Seto, Lykourgos Bougas,
418 Andrey Jarmola, and Victor M. Acosta. Diamond magnetic microscopy of malarial hemozoin nanocrystals. Phys. Rev.
419 Applied, 11:034029, Mar 2019.